

## NOTICE

THIS DOCUMENT HAS BEEN REPRODUCED FROM  
MICROFICHE. ALTHOUGH IT IS RECOGNIZED THAT  
CERTAIN PORTIONS ARE ILLEGIBLE, IT IS BEING RELEASED  
IN THE INTEREST OF MAKING AVAILABLE AS MUCH  
INFORMATION AS POSSIBLE

(NASA-TM-81715) SYNERGISTIC  
EROSION/CORROSION OF SUPERALLOYS IN PFB COAL  
COMBUSTOR EFFLUENT (NASA) 27 p  
HC A03/MF A01

N81-23245

CSCL 11F

Uncclas  
42396

G3/26

# Synergistic Erosion/Corrosion of Superalloys in PFB Coal Combustor Effluent

S. M. Benford, G. R. Zellars, and C. E. Lowell  
*Lewis Research Center*  
*Cleveland, Ohio*



Prepared for the  
Eighty-second Annual Meeting of the American Ceramic Society  
Chicago, Illinois, April 28-30, 1981

NASA

SYNERGISTIC EROSION/CORROSION OF SUPERALLOYS IN  
PFB COAL COMBUSTOR EFFLUENT

by S. M. Benford, G. R. Zellars, and C. E. Lowell

National Aeronautics and Space Administration

Lewis Research Center

Cleveland, Ohio 44135

ABSTRACT

Two Ni-based superalloys were exposed to the high velocity effluent of a pressurized fluidized bed coal combustor (PFBC). Targets were 15-cm diameter rotors operating at 40,000 rpm and small flat plate specimens. Above an erosion rate threshold (~10  $\mu\text{m}/\text{hr}$ ), the targets were eroded to bare metal. The presence of accelerated oxidation at lower erosion rates suggests erosion/corrosion synergism. Various mechanisms which may contribute to the observed oxide growth enhancement include erosive removal of protective oxide layers, oxide and subsurface cracking, and chemical interaction with sulfur in the gas and deposits through damaged surface layers.

I. INTRODUCTION

A proposed alternate method of generating electrical energy from coal requires the operation of a gas turbine in the effluent of a pressurized fluidized bed coal combustor (PFBC). The PFBC process promises to be more efficient and to produce fewer  $\text{SO}_x$  and  $\text{NO}_x$  pollutants than conventional coal-fired plants. However, a turbine operated in PFBC effluent is exposed to hot, corrosive gases and high velocity particles which can severely damage the blades. In this complex environment, a spectrum of erosion/corrosion mechanisms may produce accelerated metal attack in a synergistic manner.

The NASA Lewis Research Center PFBC program was initiated to evaluate this new concept of burning coal in an environmentally clean way, and to

provide erosion/corrosion materials data which would indicate both the extent of the problem and possible solutions. Small superalloy rotors (15 cm or 6 in. diam) were operated directly in the PFBC effluent for up to 400 hours (refs. 1 and 2), and small flat plate specimens were exposed for up to 90 hours. Additional flat plate specimens of the alloys were furnace oxidized in air at temperature for comparison with the test samples. The turbine blades exhibited accelerated oxidation, subsurface oxide penetration, and hot corrosion (sulfidation) in addition to heavy erosion. Flat plate samples were attacked by hot corrosion on the normal incidence surface (leading edge) at moderate erosion rates ( $0.5 \mu\text{m}/\text{hr}$  or  $2 \text{ mil}/100 \text{ hr}$ ), and were eroded to bare metal at higher erosion rates. This report focuses on the erosion/corrosion interaction mechanisms which might explain the accelerated corrosion observed on these superalloy airfoil and flat plate samples in the presence of erosion.

## II. EROSION/CORROSION THEORY

Erosion affects the growth rate, coherence, and composition of surface oxides by (1) decreasing the thickness of the protective oxide layer; (2) generating microcracks which may result in porosity and oxide penetration; and (3) depleting the alloy of protective oxide elements. A slight reduction in the thickness of the protective oxide layer is probably the least damaging result of erosive attack. This mechanism will be examined on the basis of a simple theoretical model, and the predicted attack rates will then be compared with experimental data. The probable results of more severe attack (crack formation and alloying element depletion) will also be discussed and compared with observations.

### (1) Coherent Oxide Growth

A coherent or protective oxide scale will be defined as an oxide which is uniform in thickness, dense, and adherent to the metal substrate. The slow, uniform bombardment of a coherent oxide surface by particles which are small in comparison with the oxide thickness will, in general, reduce the protectiveness of the oxide layer and accelerate the growth of the depletion zone. The erosion rate may be decreased by the presence of the hard oxide layer, but the metal consumption is still likely to be greater in the eroded material because of the accelerated depletion zone growth.

Figure 1(a) shows the rate of coherent oxide formation and Fig. 1(b) shows the oxide thickness as a function of time in the absence and presence of erosion, as described by the equations,

$$\dot{X}_0 = \frac{K_p}{2X_0} \quad \text{No erosion} \quad (1)$$

$$\dot{X}_{0E} = \frac{K_p}{2X_{0E}} - E \quad \text{With erosion} \quad (2)$$

where  $X_0$  is the thickness of the oxide remaining on the metal ( $\mu\text{m}$ ),  $K_p/2$  is the parabolic oxide thickness growth constant ( $\mu\text{m}^2/\text{s}$ ),  $E$  is the erosion rate ( $\mu\text{m}/\text{s}$ ),  $t$  is time (s), and  $\dot{X}_0 = dX_0/dt$ . (A similar equation is used to describe the vaporization of volatile surface oxides (ref. 3).) The surface oxide thickness removed by erosion ( $X_R$ ) is described by the linear rate equation,

$$\dot{X}_R = E \quad (3)$$

The total oxide formed (Fig. 1(b)) is equal to the amount eroded away plus the amount remaining on the surface, or  $X_{\text{total}} = X_R + X_0$ .  $X_0$  grows at a

nearly parabolic rate (dashed line) until the oxide lost by erosion is nearly equal to the amount of oxide remaining, and then approaches a limiting thickness given by,

$$x_0^{\max} = \frac{k_p}{2E} \quad (4)$$

after steady-state time,  $t_{ss}$

$$t_{ss} = \frac{k_p}{2E} \quad (5)$$

After this time, the oxide thickness is always smaller than it would have been if parabolic growth had continued, and the oxide is less protective. If the parabolic growth constant is small compared with the erosion rate, steady-state conditions are achieved quickly and the coherent oxide layer will be extremely thin according to Eq. (4). If  $x_0^{\max}$  is several angstroms and  $t_{ss}$  is less than 1 second, it is likely that, under these conditions, a coherent oxide layer may not form at all.

The depletion zone thickness ( $x_D$ ) is proportional to the total amount of oxide formed (Fig. 1(b)). When steady-state conditions have been reached, all of the oxide formed is eroded away. The oxide which remains on the surface serves as a thin diffusion barrier through which critical alloying elements are "pumped" from the substrate to the surface at a nearly linear rate. Figure 2(a) shows the relative thickness of  $x_0$  and  $x_D$  for parabolic growth and for growth in the presence of erosion.

## (2) Porous Oxides

At very high erosion rates, the initial oxide nucleation and growth processes may be disrupted (ref. 4). In the extreme case, nucleation does not take place at all, and the material is eroded to bare metal. In a less

extreme case, the growth process may proceed with the formation of atypical or porous oxides. The growth of a porous surface oxide will be governed by the equation,

$$\dot{X}_0 = a - E \quad a > E \quad (1)$$

where 'a' is the growth constant for the porous oxide in the absence of erosion ( $\mu\text{m/s}$ ). The depletion zone growth is also linear with time and is governed by the porous oxide growth constant, so that it is not significantly changed with and without erosion. Figure 2(b) shows the relative thickness of  $X_0$  and  $X_D$  for porous oxide growth in the presence and absence of erosion. Only if diffusion processes cannot keep pace with the rapid consumption of surface oxide will the depletion zone thickness be diminished in the presence of erosion.

### (3) Brittle Fracture

If the size of the bombarding particles is comparable with the oxide depth, brittle fracture may form microcrack porosity or totally expose the depletion zone in the region of impact. The effect of mechanical stress is, in this case, similar to the effect of thermal shock with resulting microcrack formation, spallation, and accelerated oxidation (refs. 5 and 6).

Figure 3 shows the erosive damage of an oxide surface by particles which appear to be about 5  $\mu\text{m}$  in size.

### (4) Composition Changes

As surface layers are eroded away and the depletion zone grows, equilibrium conditions may change to favor the formation of alternative oxides. Multilayer oxides and subsurface penetration might be expected as it becomes increasingly more difficult for the primary oxide cations to diffuse to the metal-oxide interface. Erosive exposure of depletion zones will also gener-

ate atypical oxides. In Ni-Cr-Al-based alloys which form protective chromium oxides, aluminum oxides may form in the exposed depletion zone (refs. 7 and 8). In general, metal consumption will increase as alloying element, which form the protective oxide layer are eroded away. Especially important is the fact that the eroded surface may be more susceptible to hot corrosion attack.

### III. TEST CONDITIONS

The NASA Lewis Research Center pressurized fluidized bed test facility has been described in previous reports. The combustor burns about 48 kg (30 lb) of granular coal and 2 kg (4.2 lb) of granular limestone sorbent per hour at about 6 atmospheres pressure. Air flows through the system at 300 kg/min (650 lb/min). The fluidized or suspended fuel and sorbent particles are surrounded by the flowing air, and combustion is very complete at combustion temperatures of about 1000° C (1880° F). Low temperature burning reduces the level of  $\text{NO}_x$  emissions, and the limestone sorbent reduces the level of  $\text{SO}_x$  emissions. The effluent is considered to be primarily oxidizing at test temperatures. Sulfidation may be the result of interaction with sulfur-bearing solids or with  $\text{SO}_2$  gas trapped beneath the solids.

#### (1) Solids Particles

Entrained solids in the effluent contain  $\text{SiO}_2$ ,  $\text{Fe}_2\text{O}_3$ , and aluminum-silicon compounds which reflect the nature of the coal ash, in addition to  $\text{CaSO}_4$  from the sulfated sorbent. Particles which passed through the test sections appeared to contain more sulfur-bearing species than solids which were collected by an upstream separator. Such sulfur-bearing species in deposits (e.g.,  $\text{Na}_2\text{SO}_4$  or  $\text{K}_3\text{Fe}(\text{SO}_4)_3$ ) may be highly reactive (refs. 9 and 10). Solids loadings into the test section ranged from 200 to 30,000 ppm (0.01 to 1.5 gr/SCR), and the average particle size in most tests was 10 to

15  $\mu\text{m}$ . SEM analysis of the largest particles indicates that they are highly agglomerated and may, in fact, have existed as individual smaller particles in the hot gas stream.

### (2) Turbine Test

A turbine rotor is shown in Fig. 4 and test conditions are shown in Table I. A single stator passage guided the hot gases onto about three blades at 6 percent partial admission. The blades were therefore exposed to the eroding particles for about 1.5  $\mu\text{sec}$  out of each revolution (25  $\mu\text{sec}$ ). (Actual erosive exposure time may be calculated by multiplying the test time by 0.06.) Heavy particle separation occurred both in the stator and during passage through the rotor, producing a nonuniform distribution of erosion on the blade surface. The relative gas velocity at the rotor inlet was about 300 m/s (1000 ft/s), and the gas temperature ranged from 690° to 780° C (1350° to 1450° F). Rotor materials were Alloy 713 LC (wt.% Cr-12, Al-6.1, Ti-0.6) and IN792 + Hf (wt.% Cr-12.4, Al-3.1, Ti-4.5), both nickel-base superalloys.

### (3) Flat Plate Test

A flat plate specimen exposed to the PFBC effluent for 30 hours at a solids loading of 15,000 ppm is shown (Fig. 5). The small coupons (5 x 2.5 x 1.25 cm) were mounted in a tapered tube, so that velocity varied with position along the tube. Gas pressures and temperatures were comparable to the turbine test conditions, but exposure to the solids was continuous. Gas velocities were somewhat lower (110 to 220 m/s or 360 to 720 ft/s). Lighter particles followed the gas flow around the specimen, but heavy particles penetrated the stagnation area and impact on the leading edge at 90° incidence. Particles probably impacted the sides only at shallow angles. All of the flat plate test specimens were IN792 + Hf.

## IV. RESULTS AND DISCUSSION

Most test samples were exposed to severely erosive conditions. In some turbine tests, thick oxide cover ( $\sim 20 \mu$ ) on part of a blade contrasted sharply with bare metal on other parts. It is not unexpected, then, that the simple model for coherent oxide growth appeared to predict the observed oxide and depletion zone thickness for only the least eroded samples. Oxide fracture, porosity formation, and depletion of critical alloying elements appear to dominate the damage mechanisms at these erosion rates.

#### (1) Erosion Rates

Table I shows the average blade thickness loss of the four rotors and the leading edge erosion loss of the flat plate specimens. The average surface erosion rate (Table II) was determined by dividing the average blade thickness loss (estimated at nine positions) by total test time, and this average was divided by two (for two surfaces). The rotor erosion rate is, therefore, an average over all particle impact angles, sizes, and velocities. In addition, impacted surfaces were both bare metal and oxide covered, and the average includes both ductile and brittle erosion modes. Significant erosion of the blade surfaces (20 to 120  $\mu\text{m}$ , 1 to 5 mil) reflects heavy particle separation from the gas stream. The rotor erosion and corrosion are treated as though they occur uniformly over an entire rotation, and the average erosion rate ranged from  $10^{-5}$  to  $10^{-3} \mu\text{m/s}$ .

Erosion of the flat plate specimens occurred primarily on the leading edge surface normal to the gas flow direction. Erosion on the sides was below measurable limits (2.5  $\mu\text{m}$ , 0.1 mil), and metallographic examination of the trailing edge indicated that sharp, machined corners had been retained. Therefore, the leading edge erosion rate was determined by dividing the LE-to-TE erosion loss by test time. The erosion loss of the high velocity

sample (1450  $\mu\text{m}$ , 0.6 mil) was much greater in comparison with the low velocity sample (15  $\mu\text{m}$ , 0.6 mil) than might be expected from velocity dependence alone. Since the high velocity sample was eroded to a bare-metal knife edge, ductile erosion at optimum erosion impact angles ( $\sim 30^\circ$ ) may partially account for the exceptionally heavy material loss. The average leading edge erosion rate of the flat plate specimens ranged from  $10^{-4}$  to  $10^{-2}$   $\mu\text{m/s}$  (Table II), overlapping the turbine blade erosion rate range.

## (2) Corrosion

The maximum corrosion attack depth (corrosion products plus depletion zone) was about 10 to 20  $\mu\text{m}$  for all rotors (Table I), despite a wide variation in erosion rate. However, exposure time varied and differences in average particle size, velocity, and impact angle over the blade surface strongly affected the erosion and oxide evolution in local areas. Figure 6 shows the suction side corrosion of three heavily eroded rotors (R3, R4, and R5) compared with furnace oxidized coupons. Chromium-rich oxides covered most of the suction surface on the Alloy 713LC blades (R3) after 164 hours. After 12 hours, one IN792 + Hf blade was eroded mostly to bare metal (R4) with localized nodules of alumina, and another (R5) exposed to a smaller average particle size was partly covered with mixed Al-Ti oxides. IN792 + Hf coupons formed mixed oxides of Ni, Cr, Al, and Ti in furnace tests at temperature, and the predominance of Al and Ti oxides after erosion suggests the disruption of typical oxide nucleation and growth processes at these erosion rates.

Blades removed from a less severely eroded rotor (R7) after 200 hours were almost completely covered with Al-Ti oxides (Fig. 7(a)). Oxide penetration extends into the depletion zone. Comparison with the furnace oxidized coupon (Fig. 7(c)) indicates that the attack is both accelerated and

atypical. After 400 hours, the presence of chromium sulfides in a thinner depletion zone (Fig. 7(b)) is evidence of sulfidation attack in contrast to the 480-hour, furnace-oxidized coupon (Fig. 7(d)).

Corrosion attack on the three flat plate samples primarily occurred on the leading edge of the two lower velocity samples (S1 and S2). Figure 8 shows the leading edge and one side of S1. At the leading edge the surface oxide is mixed, and the depletion zone contains sulfide particles. The oxide layer on the side of the sample is comparable in thickness and morphology to furnace oxidized coupons. Sulfur penetration appeared to occur on these samples only at the heavily eroded leading edge. The leading edge of all three flat plate samples is shown in Fig. 9. At higher gas (and particle) velocities, the corrosion attack depth decreased (S2) until erosion to bare metal dominated (S3).

### (3) Erosion/Corrosion Interaction

The presence of oxide nodules, atypical oxides, subsurface oxide penetration, and enhanced sulfidation attack on heavily eroded surfaces reflects the disruption of protective oxide growth. In the coherent oxide growth model, the rate of metal consumption is a function of both erosion rate and parabolic oxide growth rate. Disruption occurs if the time to reach steady state is short and the maximum oxide thickness is small. In order to define the conditions under which the coherent oxide growth model fails for these alloys, it is useful to calculate the steady-state parameters  $t_{ss}$  and  $x_0^{\max}$  for the test erosion rates.

Table II shows the erosion rate for each rotor and flat plate sample, ordered from low ( $10^{-5}$   $\mu\text{m/s}$ ) to high ( $10^{-2}$   $\mu\text{m/s}$ ) erosion rates. The calculated values of  $x_0^{\max}$  and  $t_{ss}$  are also shown. In general, the calculated values of  $x_0^{\max}$  are much smaller than those observed, and the

corresponding steady-state times are short. Only when the steady-state growth time is long (about 30 hr for R7) does the predicted oxide depth begin to approach the observed oxide depth. The two horizontal dashed lines in Table II define erosion rate thresholds at which the oxide growth pattern appears to change. At high erosion rates ( $10^{-3}$  to  $10^{-2}$   $\mu\text{m/s}$ ), erosion to bare metal takes place. At the lowest erosion rate ( $10^{-5}$   $\mu\text{m/s}$ ), the surface oxide was more uniform over the surface. At still lower erosion rates, oxide growth is likely to progress with nearly parabolic oxide growth kinetics (e.g., the sides of the flat plate samples). In this analysis,  $x_0^{\text{max}}$  and  $t_{ss}$  appear to serve as critical parameters which indicate the likelihood of oxide growth disruption in the presence of erosion. Figure 10 shows theoretical oxide thickness vs time calculated for IN792+Hf at several erosion rates ( $T \sim 780^\circ \text{C}$ ). The theoretical curves cross the parabolic growth curve at  $\sim 0.8 t_{ss}$ . Over this range of  $x_0^{\text{max}} < 0.1 \mu\text{m}$  and  $T_{ss} < 10,003$ , oxide growth was observed to be atypical.

The formation of microcracks by particle impact can be an important factor in the corrosion processes at moderate to heavy erosion rates. Microcrack porosity on a scale much smaller than the oxide thickness was not directly observed on these samples. However, particle impact craters and larger scale crack formation were evident on several of the rotor blades. Figure 11 shows the erosion of a turbine blade near the trailing edge tip. This is an area on the blade where heavy particle impact was especially intense. The erosion to bare metal threshold is passed within a 3-mm distance from the tip, beyond which point the oxide layer is continuous, thick, and possibly porous.

Porous oxide growth can be rapid (linear kinetics), and continuous bombardment by particles and subsequent crack formation maintains the poros-

ity. Figure 12 is a schematic of crack formation by particles impacting both an oxide and a metallic surface. Cracks propagate radially from the center of impact on the brittle oxide surface (Fig. 12(a)) (ref. 11), but propagate parallel to the surface in the case of ductile metallic surfaces (Fig. 12(b)) (ref. 12). In Fig. 13, a particle appears to have impacted an Al-Ti oxide layer, and streamers of  $\text{Al}_2\text{O}_3$  penetrate radially from the center of impact. In Fig. 14, oxides have formed in parallel cracks beneath the surface of the heavily eroded R4 blade. A significant amount of metal loss can occur if breaks run parallel beneath the surfaces, since entire layers of metal and oxide can then be successively peeled away.

Porous oxide formation may promote oxide penetration as well as enhance the likelihood of sulfidation. Figure 15 is a schematic of porous oxide formation showing evolution to these two metal attack schemes. In Fig. 15(a),  $\text{SO}_2$  diffuses through cracks in the surface oxide (ref. 13) and forms sulfides in the depletion zone. Sulfidation may occur beneath deposits of sulfur-bearing solids if there is an adequate buildup of  $\text{SO}_2$  pressure beneath the layer. In Fig. 15(b), oxygen diffuses readily through the cracks and forms a compact subsurface oxide layer with some penetration. In the last view ( $t_3$ ), the porous oxide layer has been completely eroded away, and oxide penetration continues at an accelerated pace. Sulfidation at the leading edge of a flat plate sample (FP-S1), and  $\text{Al}_2\text{O}_3$  penetration of a turbine blade (R7) are shown with the schematics as examples of each type of attack. While sulfidation and associated accelerated oxidation can surely occur in the absence of erosion, the presence of sulfidation only on the highly eroded leading edge of the flat plate samples strongly suggests enhancement in the presence of erosion. Metal loss by fluxing of the

surface and oxide breakaway can be severe once sulfidation attack has been initiated.

#### V. CONCLUDING REMARKS

Erosion/corrosion interactions are generally synergistic in a destructive manner, that is, damage is amplified. At high erosion rates, it is likely that porous oxides, thin nonprotective oxides, or faster growing oxides with a larger  $K_p$  will form. Even at low erosion rates, depletion zone growth is likely to be enhanced and net metal attack increased. The onset of accelerated oxidation is likely to be a problem at longer times, as well as sulfidation when sulfur-bearing deposits and gases are present (Fig. 16).

Although it was not observed in these tests, there appears to be an optimal value of  $K_p/E$  at which a thin but protective oxide layer may remain coherent in the presence of erosion for some time. If the average particle size is also sufficiently small, such an oxide might be useful in keeping the erosion rate low because of the harder surface. However, it is unlikely that such an oxide surface would be as effective as a properly designed coating in combating both the erosion and corrosion problems of a PFBC environment. Controlled studies of the evolution of oxides in the presence of moderate erosion would be useful in the design of these coatings.

#### VI. REFERENCES

1. G. R. Zellars, S. M. Benford, A. P. Rowe, and C. E. Lowell, The Erosion/Corrosion of Small Superalloy Turbine Rotors Operating in the Effluent of a PFB Coal Combustor, pp. 887-912 in Proceedings of the First Conference on Advanced Materials for Alternative Fuel Capable Directly Fired Heat Engines, Castine, Maine. Edited by J. W. Fairbanks and J. Stringer, CONF-790749, July-Aug. 1979.

2. R. J. Rollbuhler, S. M. Benford, and G. R. Zellars, Improved PFB Operations: 400-Hour Turbine Test Results, pp. 749-764 in Proceedings of the Sixth International Conference on Fluidized Bed Combustion, Atlanta, Georgia, Volume II. CONF-800428, 1980.
3. E. W. Haycock, Transitions From Parabolic to Linear Kinetics in Scaling of Metals, J. Electrochem. Soc., 106, 771 (1959).
4. G. C. Wood, Fundamental Factors Determining the Mode of Scaling of Heat-Resistant Alloys, Werkst. Korros., 22 [6] 491 (1971).
5. Y. Ikeda and K. Nii, Microcrack Generation and its Healing in the Oxide Scale Formed on Fe-Cr Alloys, Oxid. Met., 12 [6] 487 (1978).
6. C. A. Barrett and C. E. Lowell, Resistance of Nickel-Chromium-Aluminum Alloys to Cyclic Oxidation at 1100° and 1200° C, NASA TN D-8255, June 1976.
7. I. Kvernes and P. Kofstad, The Oxidation Behavior of Some Ni-Cr-Al Alloys at High Temperatures, Metall. Trans., 3 [6] 1511 (1972).
8. C. S. Giggins and F. S. Pettit, Oxidation of Ni-Cr-Al Alloys Between 1000° and 1200° C, J. Electrochem. Soc., 118 [11] 1782 (1971).
9. D. L. Douglass and V. S. Bhide, Mechanism of Corrosion of Structural Materials in Contact with Coal Chars in Coal Gasifier Atmospheres, University of California, Los Angeles, Cal, Semi-Annual Reports TID-23545, March 1978; TID-29304, August 1978; and SAN-0034-T3, March 1979.
10. K. E. Phillips, Energy Conversion From Coal Utilizing CPB-400 Technology, Combustion Power Co., Inc., Menlo Park, Cal., report FF-15636-30-VOL-1, March 1977.

11. M. E. Gulden, Solid Particle Erosion of High-Technology Ceramics, pp. 101-122 in Erosion: Prevention and Useful Applications. Edited by W. F. Adler, ASTM, Philadelphia, 1979.
12. N. P. Suh, An Overview of the Delamination Theory of Wear, Wear, 44, 1 (1977).
13. P. Kofstad and G1 Akesson, High-Temperature Corrosion of Nickel in  $SO_2$ , Oxid. Met., 12 [6] 503 (1978).

TABLE I. - TEST CONDITIONS AND EROSION/CORROSION RESULTS

Test <sup>a</sup>	Material	Test conditions				Erosion/corrosion results			
		Average gas temperature, °C	Average gas velocity, m/s	Average solids loading, ppm x 10 <sup>3</sup>	Test time, hr	Average erosion loss, μm	Maximum erosion loss, μm	Maximum oxide plus depletion depth, μm	Percent of C surface covered by oxide
I8T turbine									
R3	Alloy 713 LC	690	280	5.7	164	100	200	5 - 10	50
R4	IN792 + Hf	780	340	28	13	240	500	Mostly bare metal	10
R5	IN792 + Hf	780	340	27	12	100	375	5 - 10	40
R7	IN792 + Hf	770	290	1.9	400	40	150	10 - 20	90
Leading edge $\rightarrow \parallel \leftarrow$									
S1	IN792 + Hf	780	110	15	30	15	---	---	---
S2	IN792 + Hf	780	140	15	30	183	---	5	5
S3	IN792 + Hf	780	220	15	30	1450	Knife edge	Bare metal	Bare metal
								Oxidation on other surfaces < 1 μm	

where R denotes rotor number and S denotes flat plate station.  
<sup>a</sup>Relative gas velocity calculated from turbine velocity diagram.  
<sup>b</sup>Oxides > 1 μm; determined by metallography.

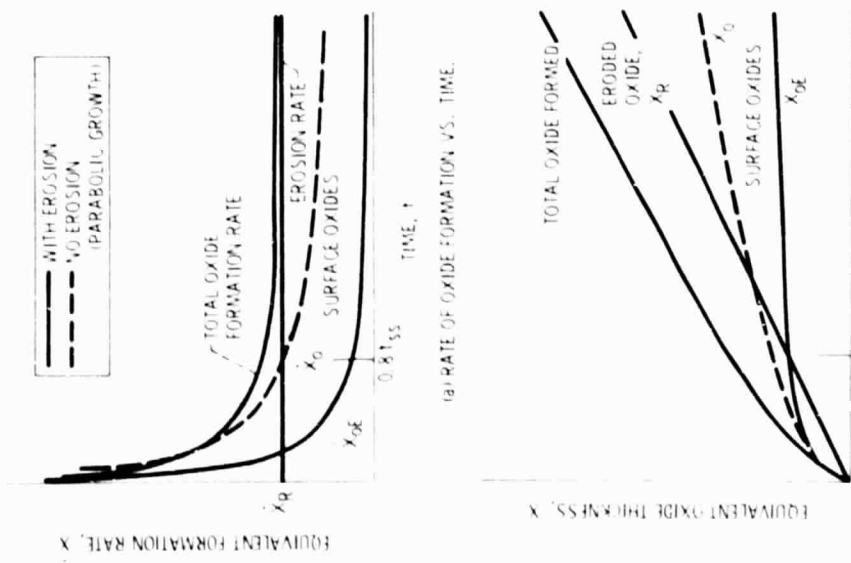
TABLE II. - DEPENDENCE OF OXIDE GROWTH PATTERN ON EROSION  
AND CORROSION RATES

	$X_R$	E	$1/2 K_p$	$X_{0\max}$ $= 1/2 K_p/E$	$t_{ss}$ $\sim 1/2 K_p/E^2$	
Test <sup>a</sup>	Average eroded depth, $\mu\text{m}$	Average erosion rate, $\mu\text{m/s}$	Parabolic growth constant, <sup>c</sup> $\mu\text{m}^2/\text{s}$	Predicted steady-state oxide thickness, $\mu\text{m}$	Predicted time to steady state, s	Observed oxide growth pattern
R7	20 <sup>b</sup>	$1 \times 10^{-5}$	$10^{-5}$	1	$10^5$	Uniform, accelerated
R3 FP-S1 R5 FP-S2	50 15 50 183	$8 \times 10^{-5}$ $1 \times 10^{-4}$ $1 \times 10^{-3}$ $2 \times 10^{-3}$	$2 \times 10^{-7}$ $10^{-5}$ $10^{-5}$ $10^{-5}$	0.003 .1 .01 .005	30 1000 10 3	Nonuniform, accelerated, porous, atypical
R4 FP-S3	120 1450	$3 \times 10^{-3}$ $1 \times 10^{-2}$	$10^{-5}$ $10^{-5}$	0.003 .001	1 .1	Bare metal

<sup>a</sup>In order of increasing erosion rate.

<sup>b</sup>Average blade thickness loss  $\div 2$ .

<sup>c</sup>From furnace tests in 1 atmosphere air.



(b) OXIDE THICKNESS FORMED AND REMAINING ON THE SURFACE OR REMOVED BY EROSION VERSUS TIME.  
Figure 1. - The effect of erosion on coherent oxide growth.

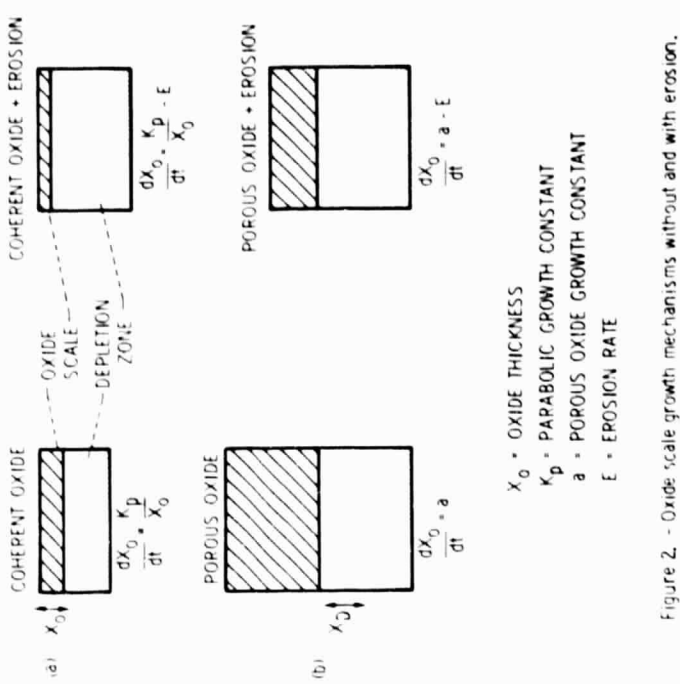


Figure 2. - Oxide scale growth mechanisms without and with erosion.

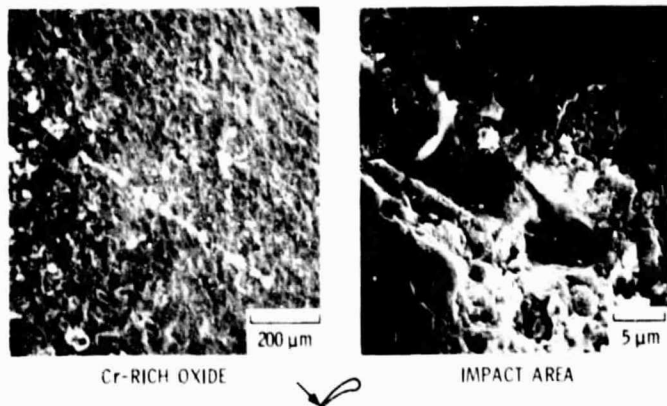


Figure 3. - Oxide removal by direct particle impact; alloy 713LC retor 3 after 164 hours at 690° C. (Average erosion depth = 50  $\mu$ m.)



Figure 4. - Integrally bladed turbine rotor.

ORIGINAL PAGE IS  
FILED IN THE CIRCUIT  
CLERK'S OFFICE  
AT THE U.S. DISTRICT  
COURT FOR THE DISTRICT  
OF COLUMBIA

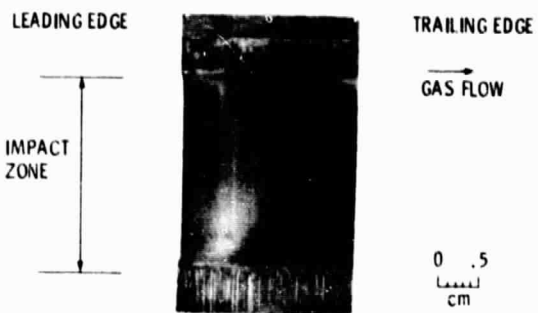


Figure 5. - Flat plate test sample (FP-S2).

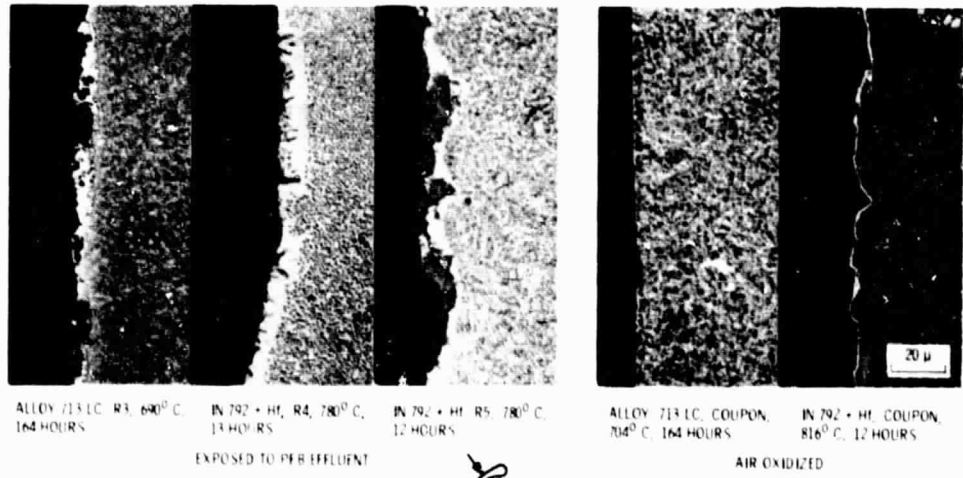


Figure 6. - Accelerated suction side oxidation of heavily eroded turbine blades; comparison with furnace oxidized coupons. (Average erosion rate, 0.3 to 10  $\mu$ m/hr.)

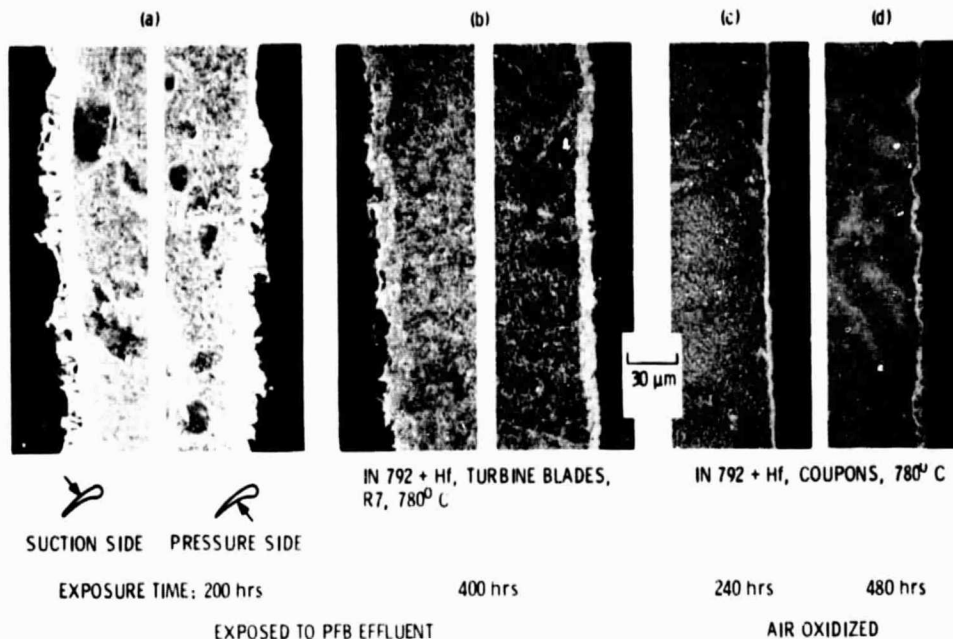


Figure 7. - Oxide penetration and sulfidation of moderately eroded turbine blades; comparison with furnace oxidized coupons. (Average erosion rate, 0.05  $\mu\text{m}/\text{hr.}$ )

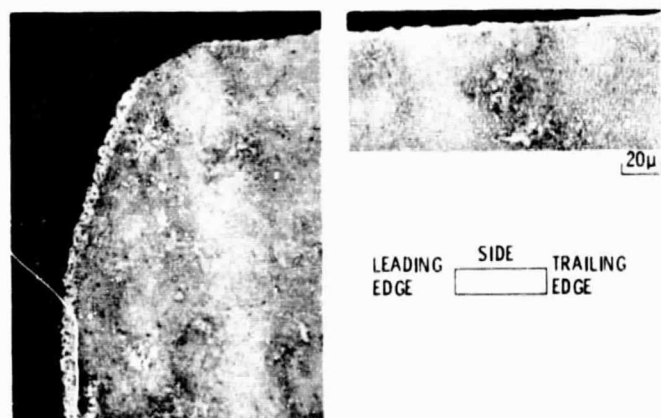


Figure 8. - Comparison of flat plate leading edge and side corrosion in PFB effluent; IN 792 + Hf flat plate sample (FP-S1) exposed at 780°C for 30 hours. (Average erosion rate, 0.5  $\mu\text{m}/\text{hr}.$ )

ORIGINAL PAGE  
OF POOR QUA.

IN-792 + HI FLAT PLATE SAMPLES, EXPOSED AT 1440° F FOR 30 hr, SOLIDS LOADING = 0.8 gr/scf

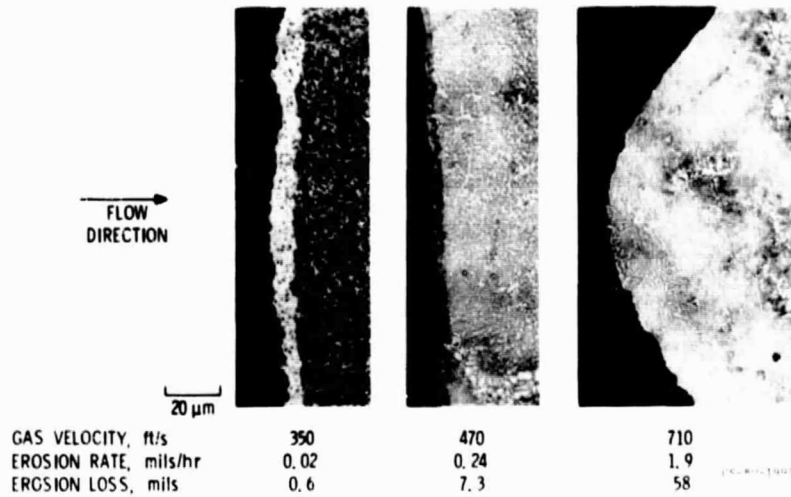


Figure 9. - Effect of gas velocity on leading edge erosion/corrosion.

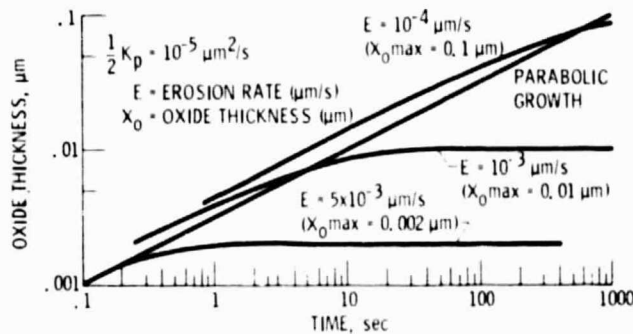


Figure 10. - Predicted coherent oxide growth rate for IN 792 + HI at several high erosion rates. Porous or a typical oxides are likely to form when  $t_{ss}$  is short and  $X_0^{\max} \ll$  particle size.

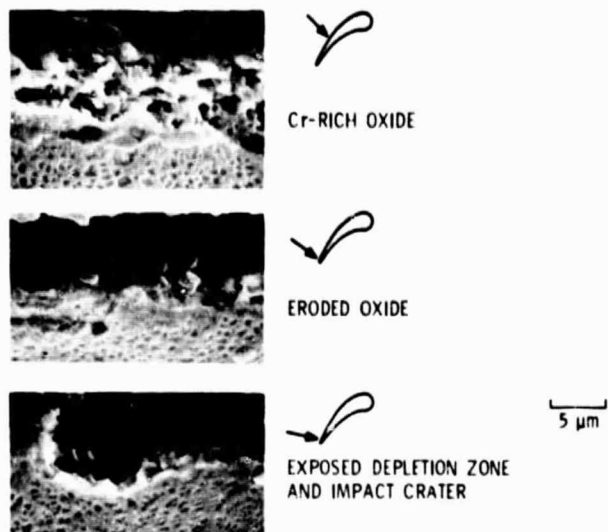


Figure 11. - Erosive exposure of depletion zone at blade trailing edge tip; alloy 713 LC rotor 3 after 164 hours at 690° C. (Average erosion depth, 50  $\mu$ m.)

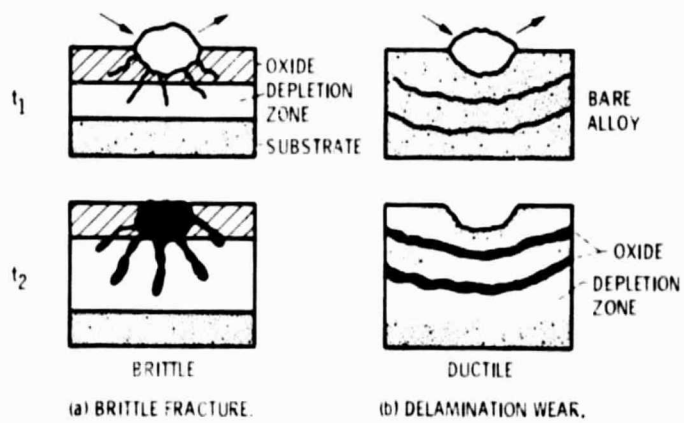


Figure 12. - Schematic models of erosive crack formation; oxide penetration occurs along the cracks.

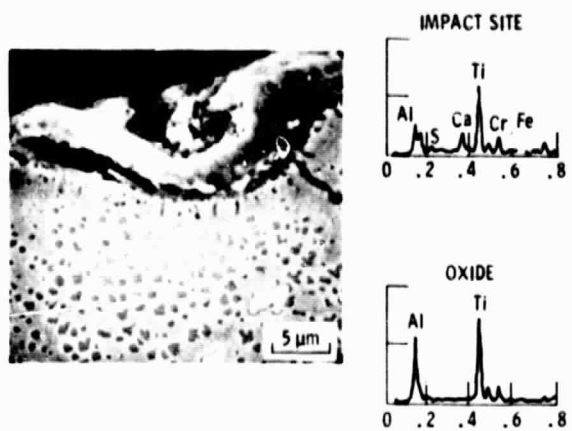


Figure 13. - Particle impact crater and radial oxide penetration; IN 792 + Hf rotor 5 after 12 hours at 780° C (average erosion depth = 50 μm).

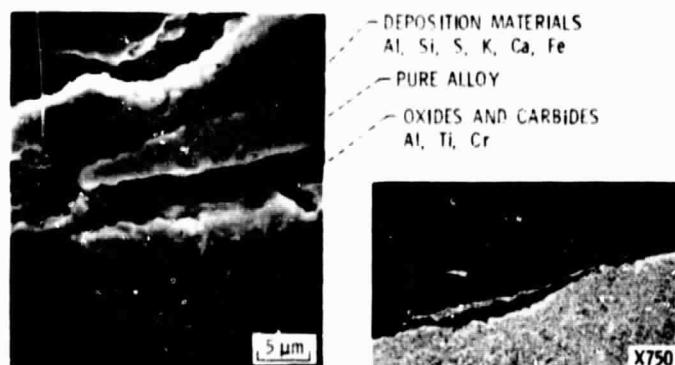


Figure 14. - Crack propagation at a subsurface oxide - alloy interface; IN 792 + Hf rotor 4 after 12 hours at 780° C (average erosion depth = 120 μm).

ORIGINAL PAGE IS  
OF POOR QUALITY

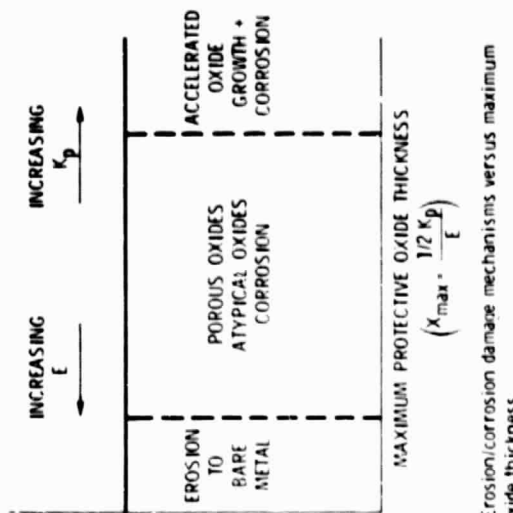
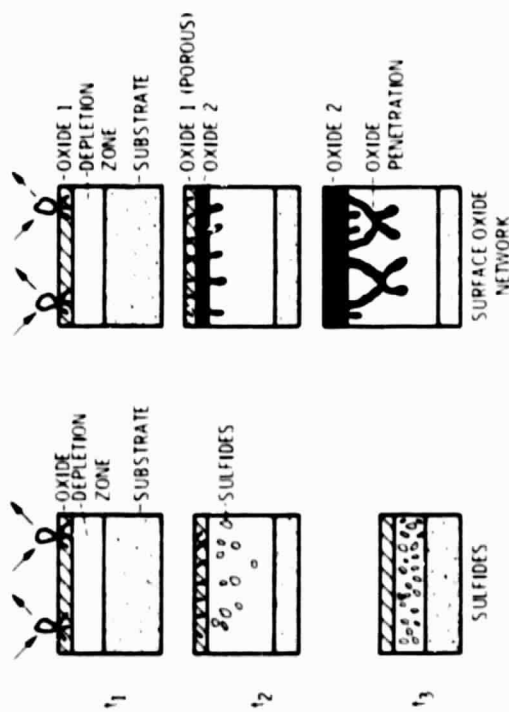
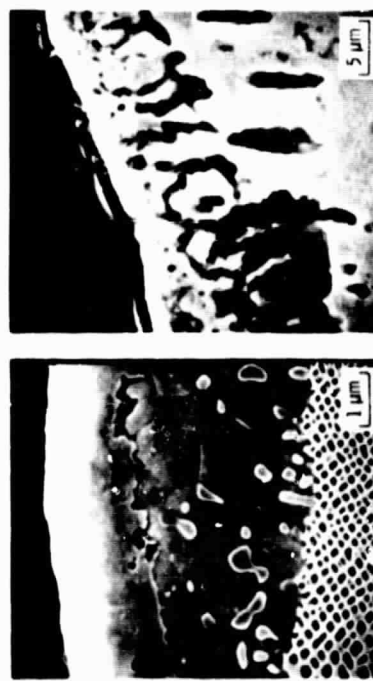


Figure 16. - Erosion/corrosion damage mechanisms versus maximum protective oxide thickness.



(a) SULFIDE PENETRATION AT THE LEADING EDGE OF THE LOW VELOCITY FLAT PLATE SAMPLE FP-S1.  
 (b) ALUMINA PENETRATION ON A ROTOR 7 TURBINE BLADE AFTER 400 HOURS.  
 Figure 17. - Models of subsurface damage after erosive cracking or removal of protective oxides and samples of each.